Geomorphology 475 (2025) 109649

Contents lists available at ScienceDirect

Geomorphology

journal homepage: www.journals.elsevier.com/geomorphology

Nonlinear modeling of river dunes: Insights in long-term evolution of dune dimensions and form roughness

W.M. van der Sande[a,*], P.C. Roos[a], T. Gerkema[b], S.J.M.H. Hulscher[a]

[a] Marine and Fluvial Systems, University of Twente, Enschede, the Netherlands

[b] Department of Estuarine and Delta Systems, NIOZ Royal Netherlands Institute for Sea Research, Yerseke, the Netherlands

ARTICLE INFO

Keywords:
River dunes
Nonlinear
Morphodynamic modeling
Flow separation
Flow roughness

ABSTRACT

River dunes are large-scale (primary) bed patterns commonly occurring worldwide. Capturing these features in process-based morphodynamic models is challenging, partly because of steep gradients at the lee side of the bedform. Here, we present a new morphodynamic model with a hydrodynamic module (solved within OpenFOAM) that is capable of capturing lee side effects such as flow separation, and with a sediment transport formulation that suppresses steep lee slopes. Model results suggest that river dunes develop as free instabilities of the flat bed, characterized by initial exponential growth. After the initial phase, dunes reach a quasi-equilibrium, with the wavenumber of the dominant topographic mode decreasing over time; this holds for a range of parameter settings. Furthermore, we show that the spatially averaged water depth – a proxy for roughness – increases with about 3–5 %; the effective roughness length increases with about 50–100 %.

1. Introduction

Sand dunes are large-scale rhythmic bed patterns occurring in rivers (as river dunes), shelf seas (as marine sand waves) and estuaries (as estuarine sand dunes; Hulscher and Dohmen-Janssen, 2005). Dune properties differ between these systems as a result of differences in water depth, flow conditions (unidirectional or oscillatory, density-driven currents) and sediment characteristics. Wavelengths of dunes range from tens of meters in rivers to hundreds of meters in seas, and they have heights on the order of meters (Lokin et al., 2022; Damen et al., 2018). Their formation can be explained either as a free instability of the flat bed (Engelund, 1970; Hulscher, 1996), or as amalgamation of smaller-scale instabilities (Fourrière et al., 2010; Charru et al., 2013). In the discussion, we reflect on these two formation hypotheses in the context of river dunes.

Linear stability models are based on the hypothesis that dunes originate as a free instability, and they have been widely applied to explain the formation stage of bedforms other than river dunes and marine sand waves, such as sand ripples (Blondeaux, 1990), shoreface-connected ridges (Trowbridge, 1995), and tidal sandbanks (Huthnance, 1982). Linear stability models are suitable to systematically investigate the underlying mechanisms through extensive sensitivity analyses, because they are flexible and computationally cheap. However, analyses remain limited to the initial stage of formation in which amplitudes are small compared to the water depth. As a consequence, linear models only yield growth and migration rates, and in particular the preferred wavelength (for which the growth rate attains its maximum; Dodd et al., 2003).

Nonlinear models are, in contrast to linear stability models, capable of describing bedforms in the finite amplitude regime, hence yielding (quasi-)equilibrium dune height, length, and shape. Within the class of nonlinear models, there is a distinction between weakly nonlinear models and (strongly) nonlinear models. Weakly nonlinear models are an efficient method that extend the linear analysis to second (Ji and Mendoza, 1997) or third order (Colombini and Stocchino, 2008), the latter being capable of describing amplitude growth towards equilibrium for parameter values around the onset of instability. Strongly nonlinear dune models use numerical integration to solve the system of equations, and are further discussed herein.

In riverine settings, a primary challenge for nonlinear models is the description of hydrodynamic lee side effects. That is, flow over the steeper lee side of the dune forms a wake with adverse pressure gradients, giving rise to increased turbulence and potentially flow separation (Kwoll et al., 2016; Kostaschuk, 2000). These wake effects increase the form roughness, which is the decelerating effect of dunes on the flow in addition to skin friction (Van Rijn, 1984). In depth-averaged flow

* Corresponding author.
E-mail address: w.m.vandersande@utwente.nl (W.M. van der Sande).

https://doi.org/10.1016/j.geomorph.2025.109649
Received 4 October 2024; Received in revised form 3 February 2025; Accepted 4 February 2025
Available online 12 February 2025

models (which do not resolve dunes), wake effects are usually parameterized by an increased value of the roughness coefficient, which is often used as calibration parameter (e.g., Davies and Robins, 2017) or determined from dune characteristics (Van Rijn, 1984; Lefebvre and Winter, 2016).

Hence, much of past nonlinear river dune model developments have focused on finding satisfactory descriptions of turbulence and sediment transport in the wake, either through parametrization of wake effects (Paarlberg et al., 2009), or by detailed process-based modeling (e.g., Giri and Shimizu, 2006). An essential element for a satisfactory process-based description of flow in the wake of dunes is non-hydrostaticity of the flow (Lefebvre et al., 2014). That is, for an accurate description of flow over dunes and to quantify the form roughness of dunes, non-hydrostatic pressure variations need to be accounted for. Therefore, the hydrostatic balance, assumed in shallow flow modeling, should not be applied, although this makes the flow solution computationally more expensive.

Within the class of nonlinear models, two different types of flow descriptions can be recognized: those based on the Reynolds-Averaged Navier Stokes (RANS) equations, and Large Eddy Simulations (LES; Nabi et al., 2013; Sotiropoulos and Khosronejad, 2016; Liu et al., 2019). LES models yield a detailed picture of (transient) flow over dunes, but require three-dimensionality and small timesteps, and hence are computationally expensive and limited to small spatiotemporal scales (order of meters and hours, respectively; e.g., Nabi et al., 2013). RANS-based models, on the other hand, are computationally cheaper and do not necessarily require a transient flow solution as RANS models solve the flow averaged over a turbulent timescale.

However, also RANS-based morphodynamic models for river dune evolution are often applied on a small spatiotemporal domain (order of meters and hours, respectively; Giri and Shimizu, 2006; Niemann et al., 2011; Doré et al., 2016), or alternatively on long domains but relatively short timescales (Giri et al., 2015). Model studies of evolution of a river dune field from a flat bed to quasi-equilibrium on a large spatiotemporal scale are lacking.

Marine sand waves are formed by similar physical processes as river dunes (Vittori and Blondeaux, 2020). Simulations on large spatiotemporal scales of these bedforms do exist (Van den Berg et al., 2012), and have been employed in a wide array of idealized settings; that is, to isolate a limited number of processes to find relations between these processes and sand wave characteristics (Campmans et al., 2018; Damveld et al., 2020). However, a limitation of these long-term dune evolution models is that they do not account for nonhydrostatic phenomena.

In summary, current nonlinear dune models are either limited to small spatiotemporal scales (Giri and Shimizu, 2006; Niemann et al., 2011; Doré et al., 2016), or based on the hydrostatic pressure assumption, thus not adequately representing the dune-induced form roughness (Paarlberg et al., 2009; Van den Berg et al., 2012; Campmans et al., 2018). Hence, insights of long-term evolution of a dune field from a model capable of describing wake effects are missing. Also the long-term development of form roughness as dunes grow is not yet described.

The aim of this study is twofold: first, to develop a process-based model that describes dune growth towards dynamic equilibrium; second, to study the sensitivity of the morphodynamic evolution to environmental parameters, in particular initial depth and flow velocity. The parameter setting reflects lowland rivers, characterized by small Froude numbers and small relative roughness height values. Furthermore, we investigate and quantify the form roughness as dunes evolve. To this end, we present and analyze a novel nonlinear morphodynamic 2DV (i.e., two-dimensional vertical) river dune model, which uses the OpenFOAM software to solve the nonhydrostatic flow field, and hence is capable of describing wake effects. The flow is forced by a constant discharge, whereas the water depth changes as dunes develop. We couple the flow to bed evolution through the morphodynamic loop, and show long-term simulations to find sand dune patterns in a dynamic quasi-equilibrium. Results show detailed flow characteristics over a dune field, and the morphodynamic evolution of sand dunes from a slightly perturbed bed. Furthermore, we show the water depth and the development of modeled form roughness as dunes grow.

From here, we continue with a model description (Section 2) and solution method (Section 2.6), followed by the results (Section 3), and lastly by the discussion and conclusion (Sections 4 and 5, respectively).

2. Model formulation and solution

2.1. Geometry and assumptions

As shown in Fig. 1, we adopt a 2DV model domain (and hence assume uniformity in the lateral direction), with an inclined coordinate system with energy slope i_b: the x-coordinate points in longitudinal direction parallel to the water surface (with river flow in the positive x-direction), and the z-coordinate points upward perpendicularly to the water surface. The longitudinal boundaries are periodic over length L; the bed is defined as $z = -H + h$, with $h = h(x, t)$ representing the dune topography as a function of x and time t, and $H = H(t)$ the spatially averaged water depth. The initial water depth is given by $H(0) = H_0$ and the initial domain-averaged flow velocity by $U_{\mathrm{res},0}$. Finally, the surface is represented by a rigid lid at $z = 0$, and thus horizontal pressure variations reflect the hydrostatic pressure variations that would be present if there were an undulated free surface (see e.g., Xie et al., 2013). The resulting horizontal pressure variations correspond to a free surface elevation range of about one centimeter in the simulations, hence justifying the rigid lid assumption.

We neglect effects of wind and waves, and focus here on river flow, which is driven by a constant specific discharge. The specific discharge is maintained by a (possibly varying) water depth $H(t)$, whereas the barotropic pressure gradient (following from the energy slope i_b) remains constant throughout the simulation (e.g., Paarlberg et al., 2009). Sediment is assumed noncohesive and of uniform grain size, and transported as bed load; we neglect suspended sediment transport. This is motivated by bed load transport being essential in order to investigate the formation and dynamic evolution of sand dunes, whereas suspended sediment transport is not, although it does play a role in damping the growth mechanism.

Our model solves the morphodynamic loop, coupling bed evolution to sediment transport, which follows from the flow field, which in turn follows from the bed topography. Hereafter, we describe the model in terms of these different parts of the morphodynamic loop.

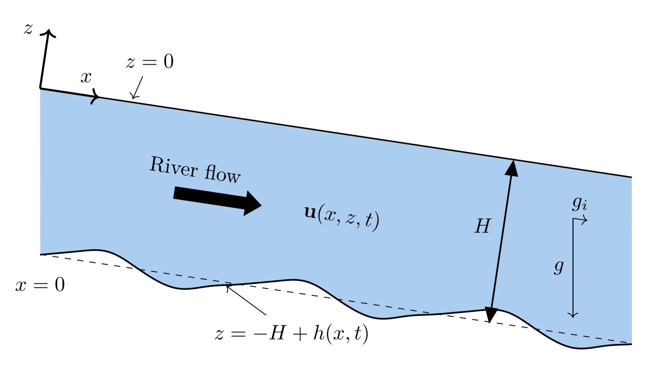

Fig. 1. Overview of the 2D*V* model domain with domain length L and mean depth $H = H(t)$. The coordinate system is tilted (note that the tilt is strongly exaggerated for visualization) such that the x-coordinate is parallel to the average energy slope i_b. This energy slope gives rise to the streamwise gravity-induced forcing $g_i \approx g i_b$, resulting in a spatiotemporally varying flow field $\mathbf{u} = (u, w)$. The bed is located at $z = -H + h$, with bed topography h; the surface is represented by a rigid lid at $z = 0$.

2.2. Bed evolution

The unknown of primary interest in this study is the bed topography h, the evolution of which follows from the Exner equation, expressing conservation of sediment:

$$(1-p_{\mathrm{or}})\frac{\partial h}{\partial t}+\frac{\partial q}{\partial x}=0. \tag{1}$$

Here, we have introduced the volumetric bed load sediment transport per unit width $q(x,t)$ (in $\mathrm{m}^2\mathrm{s}^{-1}$), and the bed porosity $p_{\mathrm{or}}=0.4$. Hence, to obtain the evolution of h, we need the spatiotemporal sediment transport pattern q.

2.3. Sediment transport

Bed load sediment transport is modeled by a power law of the bed shear stress with a slope correction (Meyer-Peter and Müller, 1948; Bagnold, 1956):

$$q=\alpha|\tau_b|^{\beta}\left(\frac{\tau_b}{|\tau_b|}-\alpha_{\mathrm{bs}}\lambda\frac{\partial h}{\partial x}\right). \tag{2}$$

Here, $\alpha=1.46e-5\ \mathrm{m}^{7/2}\mathrm{s}^2\ \mathrm{kg}^{-3/2}$ is the proportionality coefficient, $\beta=1.5$ the exponent, and $\alpha_{\mathrm{bs}}\lambda$ a slope correction to be specified below. Furthermore, τ_b is the bed shear stress (in N m^{-2}), which is defined according to

$$\frac{\tau_b}{\rho}=(\mathscr{T}_{\mathrm{Re}}\cdot\mathbf{n}_b)\cdot\mathbf{t}_b \qquad \text{at } z=-H+h. \tag{3}$$

Here, $\rho=1000\mathrm{kg\,m}^{-3}$ is the water density, and $\mathscr{T}_{\mathrm{Re}}$ the Reynolds stress tensor; $\mathbf{n}_b$ and $\mathbf{t}_b$ are the unit vectors perpendicular and tangential to the bed, respectively. The slope correction $\alpha_{\mathrm{bs}}\lambda$ is a function of the local bed slope, such that larger slopes lead to increasingly more slope-induced sediment transport (Lesser et al., 2004). It is approximated with a Taylor series in powers of the local bed slope:

$$\lambda=\sum_{l=1}^{N}\frac{c_l}{l!}\left(\frac{\partial h}{\partial x}\right)^{l-1},$$

$$c_l=\frac{\partial^l f_\lambda}{\partial x^l}(0),\qquad f_\lambda=\frac{\tau_b}{|\tau_b|}\left[1-\frac{\tan\Theta\sqrt{\left(\frac{\partial h}{\partial x}\right)^2+1}}{\tan\Theta+\frac{\partial h}{\partial x}\frac{\tau_b}{|\tau_b|}}\right]. \tag{4}$$

The function f_λ as originally reported by Lesser et al. (2004) has an asymptote at $\frac{\tau_b}{|\tau_b|}\frac{\partial h}{\partial x}=-\tan\Theta$. This implies that sediment transport is increasingly enhanced towards lee slopes of angle $\Theta=30^\circ$, which is the angle of repose of wet sand. This function f_λ avoids unrealistically large slope angles without having to include a correction for avalanching, such as done by Niemann et al. (2011). By adopting a Taylor approximation of f_λ (truncated at $N=15$, see Fig. 2), we avoid the vertical asymptote, thus ensuring numerical tractability in the vicinity of the asymptote, and allowing for a semi-implicit numerical scheme because $\frac{\partial h}{\partial x}$ can be taken outside brackets (see Appendix A). For weak slopes ($|\frac{\partial h}{\partial x}|\ll 1$), Eq. (4) reduces to $\lambda=\frac{1}{\tan\Theta}\approx 1.7$, which is consistent with earlier linear stability studies (Hulscher, 1996; Van der Sande et al., 2021). Lastly, the parameter $\alpha_{\mathrm{bs}}=2.5$ is the slope parameter, which is often used for model calibration (e.g., Krabbendam et al., 2021). This added slope effect is a consequence of calculating the sediment transport with the shear stress evaluated at the bed, instead of slightly above it. That is, bed-load transport takes place in a layer of finite thickness above the bed, and accounting for this would result in smaller growth rates (Colombini, 2004).

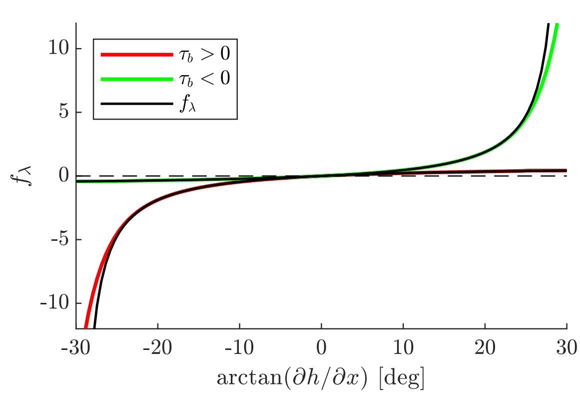

Fig. 2. Bed slope correction function for sediment transport f_λ and the Taylor approximations for $\tau_b>0$ and $\tau_b<0$; see Eq. (4).

2.4. Hydrodynamics

The bed shear stress in Eq. (3) follows from the flow solution. Here, we adopt a quasi-stationary approach, justified by the morphologic changes being much slower than hydrodynamic changes (Dodd et al., 2003). This allows us to separate the timescale of the flow from the morphodynamic timescale. Hence, we solve the steady incompressible nonhydrostatic 2DV RANS equations over a fixed topography:

$$\nabla\cdot\mathbf{u}=0; \tag{5a}$$

$$(\mathbf{u}\cdot\nabla)\mathbf{u}=-\frac{1}{\rho}\nabla p-\mathbf{F}+\nu\nabla^2\mathbf{u}+\nabla\cdot\mathscr{T}_{\mathrm{Re}}. \tag{5b}$$

Here, $\mathbf{u}=(u,w)^T$ is the Reynolds-averaged flow velocity vector in the 2DV plane (see Fig. 1; the superscript ^{T} denotes the transpose), with u the horizontal and w the vertical velocity component. Furthermore, $\nabla=\left(\frac{\partial}{\partial x},\frac{\partial}{\partial z}\right)^T$ is the 2DV nabla operator; p is the nonhydrostatic pressure (defined as the actual pressure minus the hydrostatic pressure), and $\mathbf{F}=(g_i,0)^T$ is the (steady) barotropic forcing, with $g_i=gi_b/\sqrt{i_b^2+1}\approx gi_b$ the gravity component in the x-direction (see Fig. 1). We choose the value of i_b (and thus of g_i) such that initially we obtain the prescribed domain-averaged horizontal velocity $U_{\mathrm{res},0}$. Initially, the depth is given by $H(0)=H_0$ (see Table 1); throughout the simulation the specific discharge remains constant, and H is adapted to compensate for changes in the flow velocity. Furthermore, $\nu\approx 1.0\times10^{-6}\,\mathrm{m}^2\mathrm{s}^{-1}$ is the kinematic viscosity of water.

We model the (2DV) Reynolds stress tensor with the Boussinesq hypothesis (e.g., Kundu et al., 2016) according to:

$$\mathscr{T}_{\mathrm{Re}}=2AS-\frac{2}{3}kI,\qquad S=\frac{1}{2}\left(\nabla u+(\nabla u)^T\right). \tag{6}$$

Here, I is the 2×2 identity matrix, S is the strain rate tensor, k the turbulent kinetic energy and A the eddy viscosity (in $\mathrm{m}^2\mathrm{s}^{-1}$). k and A are both determined by the turbulence closure, for which we use the k-ω model. Our motivation for choosing k-ω is because it is generally more accurate near walls and for flows with adverse pressure gradients compared to the k-ϵ turbulence closure (Bardina et al., 1997; Wilcox, 1993).

Let us finally turn to the boundary conditions. In addition to the spatially periodic boundary condition at $x=0,L$, we impose at $z=0$ zero shear stress ($A\frac{\partial u}{\partial z}=0$) and no flow ($w=0$, representing a rigid lid); at the bed we impose a no-slip condition ($\mathbf{u}=0$), which is imposed through the Nikuradse roughness height. The Nikuradse roughness height k_s is set to a constant value of 0.01 m, as such parameterizing the presence of smaller-scale ripples (Van Rijn, 1984). The flow is hydraulically rough in all simulations shown here, meaning that the dimensionless roughness height $k_s^+=\frac{u_\tau k_s}{\nu}>100$, with shear velocity $u_\tau=\sqrt{\frac{\tau_b}{\rho}}$.

Table 1
Parameters of the model with the values used.

Symbol	Description	Value	Units
L	Domain length	400, 1200[a]	m
ν	Kinematic viscosity of water	1.0e-6	m^2s^{-1}
α	Bed load transport coefficient	1.46e-5	$m^{7/2}s^2\ kg^{-3/2}$
α_{bs}	Slope transport parameter	2.5	[−]
β	Bed load transport exponent	1.5	[−]
Θ	Angle of repose of wet sand	30	degrees
ρ	Water density	1000	$kg\cdot m^{-3}$
p_{or}	Bed porosity	0.4	[−]
k_s	Nikuradse roughness height	0.01	m

Symbol	Cases	I[b]	II	III	IV	V	Units
$U_{res,0}$	Domain-avg. flow velocity[c]	0.8	0.8	0.8	0.6	1.0	ms^{-1}
H_0	Mean water depth[c]	7	4	10	7	7	m
i_b	Energy slope[d]	2.1	4.2	1.3	1.2	3.2	$\times 10^{-5}$ [−]
Fr	Froude number[e]	0.097	0.13	0.081	0.072	0.12	[−]
k_s^*	Relative Nikuradse roughness[f]	1.4	2.5	1.0	1.4	1.4	$\times 10^{-3}$ [−]

[a] For constructing the linear growth curve (see Section 3.3).
[b] Reference case.
[c] As defined initially.
[d] Depending on other parameters
[e] $\mathrm{Fr} = U_{res,0}/\sqrt{gH_0}$.
[f] $k_s^* = \dfrac{k_s}{H_0}$.

Lastly, for the nonhydrostatic pressure it suffices to set a datum at an arbitrary point in the domain; when presenting the results we set the domain-average to zero.

2.5. Initial topography

As initial topography, we impose a randomly perturbed bed according to (see e.g., blue line in upper panel of Fig. 6):

$$h(x,0) = \Re\left\{\sum_{n=1}^{N_c} \widehat{h}_{n,0}\exp(k_{b,n}x)\right\}, \qquad k_{b,n} = 2\pi n/L. \tag{7}$$

Here, $\Re\{\cdot\}$ denotes the real part, and $\widehat{h}_{n,0}$ is the initial complex bed amplitude of mode n, and its modulus $|\widehat{h}_{n,0}|$ is nonzero only for $n \in \{1, 1+n_{step}, 1+2n_{step}, \ldots, N_c\}$; the others are set to zero. Furthermore, each nonzero mode gets the same initial modulus, with $\sum_n |\widehat{h}_{n,0}| = C$, with $C = 0.3m$ a constant, which is small enough for the initial configuration to satisfy the condition for linearity in the bedform amplitude: $\max_x \frac{|h|}{H} \ll 1$. The initial dynamics can thus be regarded as linear dynamics, implying it can be used to obtain a growth curve from this nonlinear model (see Section 3.3). We note that in the morphodynamic system, a mode can only excite higher modes than itself, that is, if we were to exclude the first mode from the initial condition, this mode will also not show up in the morphodynamic evolution – hence we require that $|\widehat{h}_{1,0}| > 0$. Lastly, the initial phase of each mode is chosen randomly: $\arg(\widehat{h}_{n,0}) \in [-\pi, \pi)$.

2.6. Solution method

Flow over a given topography is solved within the OpenFOAM software (Weller et al., 1998), from which the bed shear stress is extracted using Eq. (3) to calculate the sediment transport and bed evolution using Eqs. (2) and (1), respectively.

The horizontal coordinate is discretized with the same equidistant horizontal grid (with space step Δx) for flow as for sediment transport and bed evolution. We note that our choice for $\Delta x = 2$ m reflects a dune setting; modeling superimposed ripples would require a much finer grid. Furthermore, a varying morphodynamic timestep Δt_m is used (depending on numerical stability criteria):

$$x_j = \left(j + \frac{1}{2}\right)\Delta x, \qquad j = 0, \ldots, J = \frac{L}{\Delta x} - 1,$$
$$t_m = \sum_{m'=0}^{m-1} \Delta t_{m'}, \qquad m = 0, 1, \ldots \tag{8}$$

The vertical grid is non-equidistant with constant stretching rate $\delta > 1$:

$$\Delta z_i = \delta \Delta z_{i-1}, \qquad i = 0, \ldots, I-1. \tag{9}$$

Here, I is the number of cells in the vertical, and Δz_0 and Δz_{I-1} are the cell height of the wall-adjacent cell and the uppermost cell, respectively. Defining the total expansion ratio $M = \frac{\Delta z_{I-1}}{\Delta z_0}$ leads to the following expression for any cell height Δz_i:

$$\Delta z_i = (H-h)\delta^i \frac{\delta - 1}{\delta^I - 1}, \qquad \delta = M^{\frac{1}{I-1}}. \tag{10}$$

Hence, with this method the vertical grid is determined by the expansion ratio M, the number of vertical grid cells I, and the local water depth $H - h$.

Lastly, for an accurate description of the bed shear stress, it is required that the center of the wall-adjacent cell lies within the log-law region of the boundary layer:

$$\frac{\Delta z_0}{2}\frac{u_\tau}{\nu} \le 200. \tag{11}$$

This is achieved with $M = 50$ and $I = 70$ for Case I (reference case, see Table 1), which corresponds to a stretching rate of $\delta = 1.0583$.

The Exner Equation (1) is numerically integrated through a finite difference method. Herein, we recognize two contributions within the sediment transport q (see Eq. (2)): the first contribution yields a hyperbolic term after substitution in the Exner equation and is solved with a Total Variation Diminishing (TVD) upwind scheme; the second contribution (due to the slope correction) yields a parabolic term after substitution and is solved through a semi-implicit scheme (see Appendix A). Appendix B contains a study to the numerical convergence of the model setup.

3. Results

3.1. Overview of simulations

First, in Section 3.2, we visualize the flow over a dune pattern generated by our model (a snapshot from our reference morphodynamic model simulation, see Table 1), consisting of flow velocity (in both x and z-direction), turbulent kinetic energy, and nonhydrostatic pressure. Furthermore, we focus on a location displaying flow separation.

Second, in Section 3.3, we show the initial growth and migration rates as obtained from the initial dynamics in our nonlinear model, to qualitatively compare our nonlinear model with linear stability models. We do so for variations in two different parameters (see Table 1): initial depth H_0 and initial depth-averaged flow velocity $U_{res,0}$, which are chosen because they are key parameters in the physical system. These two parameters are varied one-at-a-time with a higher and a lower value, hence in total comprising five runs. The Froude number ranges from $F_r = \frac{U_{res,0}}{\sqrt{gH_0}} = 0.072$ to 0.13, corresponding to subcritical flow representative of lowland rivers. Furthermore, the relative Nikuradse roughness height ranges from $\frac{k_s}{H_0} = 1.0 \times 10^{-3}$ to 2.5×10^{-3}.

Third, in Section 3.4, we investigate the nonlinear development of sand dunes in the spatial domain for the reference case (Case I), and the sensitivity to variations in initial depth H_0 and initial flow velocity $U_{\mathrm{res},0}$ in the frequency domain (through a Fourier transform). The former shows the evolution of the topography; the latter shows the development of topographic wave modes. The variations in parameter values are the same as for the analysis of the initial dynamics (see above).

Finally, we estimate the effective roughness which increases as a result of dune evolution in Section 3.5.

3.2. Flow pattern over dunes

Flow decelerates over troughs, and accelerates over crests (Fig. 3a); the vertical flow velocity is generally directed downward in the lee of the dune, and upward at the stoss side (Fig. 3b). Nonhydrostatic pressure (Fig. 3d) is higher over troughs than over crests, which corresponds with the flow field through Bernoulli's principle. The nonhydrostatic pressure varies primarily in the horizontal direction; vertical variations are subtle though essential for the lee side flow dynamics.

The lee sides of all dunes show enhanced turbulent kinetic energy k (Fig. 3c), this is more pronounced for the leftmost trough shown in Fig. 3. Fig. 3 (e) and (f) zoom in on this trough, and show a flow

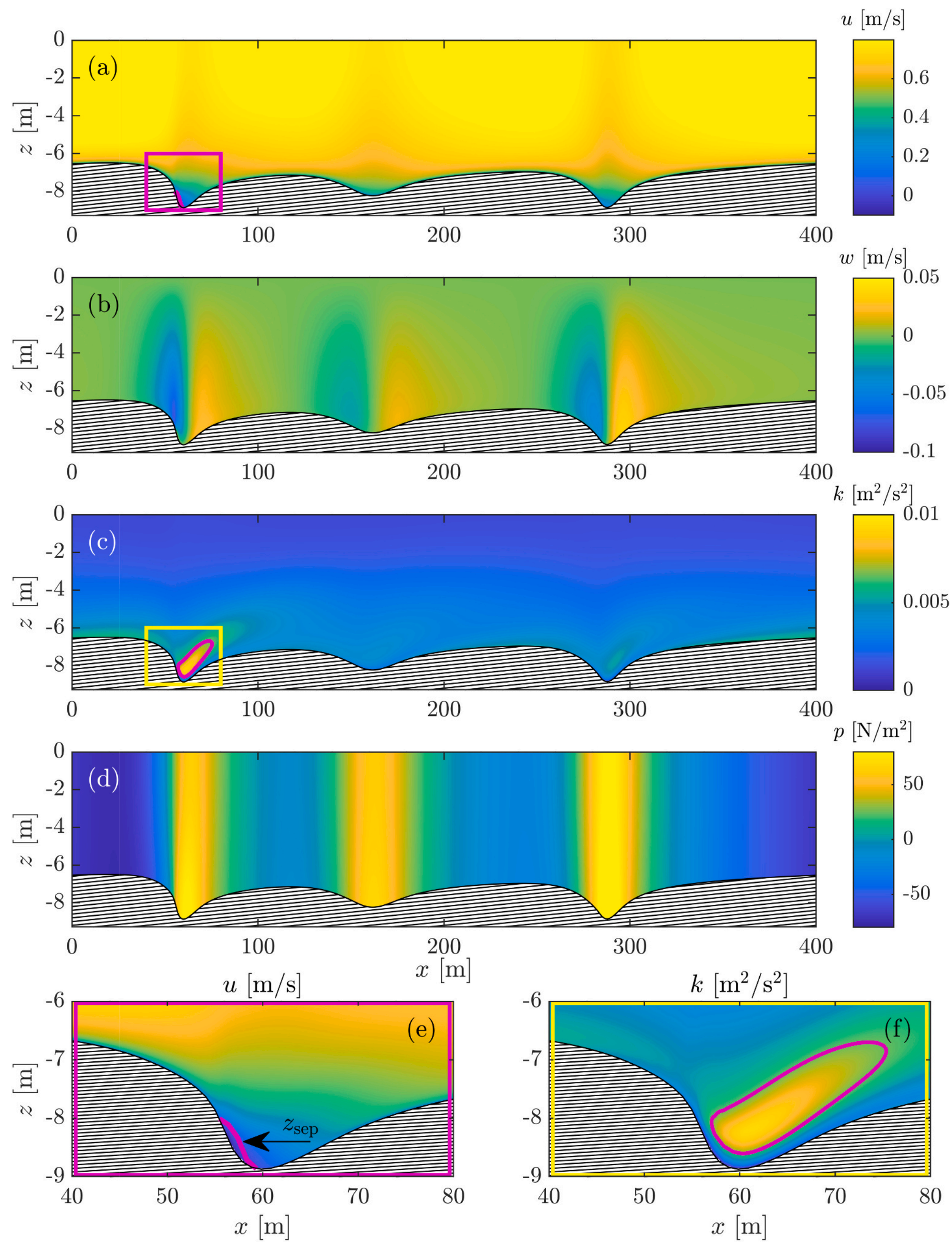

Fig. 3. Flow field for Case I (reference case) at $t = 448$ d (corresponding to $t^* = 5.6$ in nondimensional time, see Section 3.3). From top to bottom: (a) horizontal flow velocity u, (b) vertical flow velocity w, (c) turbulent kinetic energy k and (d) nonhydrostatic pressure p. Lower panels zoom in on a dune showing (e) flow separation and (f) corresponding increased turbulent kinetic energy; flow separation zone and wake are depicted by the purple lines. (For interpretation of the references to color in this figure legend, the reader is referred to the web version of this article.)

separation zone and an accompanying increase in turbulent kinetic energy. Flow separation turns out to occur over one dune in this snapshot; other dunes do not display flow separation, probably because their lee-side angles are less steep (Lefebvre et al., 2014). The upper limit of the region of flow separation, denoted by z_{sep} and indicated with the purple line in Fig. 3 (a) and (e), is defined as follows (Lefebvre et al., 2014; Paarlberg et al., 2007):

$$\int_{-H+h}^{z_{\mathrm{sep}}} u\,\mathrm{d}z = 0. \tag{12}$$

Furthermore, the turbulent wake – outlined with purple in panels showing the turbulent kinetic energy k – is defined as the contour of 70 % of the maximum turbulent kinetic energy (Lefebvre et al., 2014). The two of the three troughs that do not exhibit separation of flow, also do not have a turbulent wake according to this definition, as the turbulent kinetic energy in those troughs is much smaller. This likely reduces the overall form roughness (see also Section 3.5).

3.3. Initial growth and migration

The initial growth can be described – conform linear stability models (e.g., Richards, 1980; Hulscher, 1996) – with a growth curve, which shows the growth rate as a function of the topographic wavenumber k_b. To this end, we first write the bed topography as a Fourier series, similar as in Eq. (7):

$$h(x,t) = \Re\left\{ \sum_{n=0}^{N_x/2} \widehat{h}_n(t)\exp\left(k_{b,n}x\right) \right\}, \qquad k_{b,n} = 2\pi n/L. \tag{13}$$

Here, $\widehat{h}_n = \widehat{h}_n(t)$ is the complex amplitude function corresponding to wavenumber $k_{b,n}$. In the linear regime, where $\max_x|h|/H \ll 1$, the individual topographic modes evolve independently according to (for derivation, see e.g., Van der Sande et al., 2023):

$$\frac{\partial \widehat{h}_n}{\partial t} = \gamma_n \widehat{h}_n \qquad \rightarrow \qquad \gamma_n = \frac{1}{\widehat{h}_n}\frac{\partial \widehat{h}_n}{\partial t}. \tag{14}$$

Here, $\gamma_n = \gamma_{n,r} + \mathrm{i}\gamma_{n,i}$ is the complex growth rate corresponding to wavenumber $k_{b,n}$, with its real part $\gamma_{n,r}$ constituting the growth rate of the amplitude and the imaginary part containing the migration rate $c_{\mathrm{mig}} = -\gamma_i/k$. Hence, for an initial bed level change $\partial\widehat{h}_n/\partial t$ of an arbitrary topography $\widehat{h}_n$, we can estimate the complex growth rate γ_n.

The results are shown for each case as defined in Table 1 (Fig. 4), and

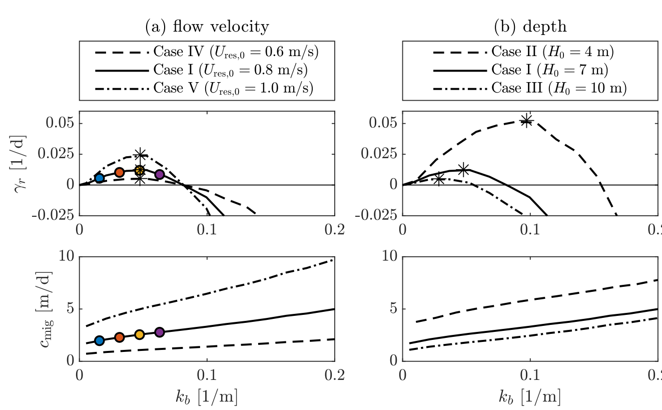

Fig. 4. Growth rate γ_r and migration rate c_{mig} as a function of topographic wave number k_b. Solid line is for Case I (reference case), dashed lines for the lower parameter value, and dash-dotted lines for the higher parameter value (see Table 1); on the left $U_{\mathrm{res},0}$, on the right H_0. Derived from our model with domain length $L = 1.2$ km; initial condition as in Eq. (7) with $n_{\mathrm{step}} = 3$ and largest topographic wavenumber of $k_b = 0.29\mathrm{m}^{-1}$. Colored circles correspond to the modes shown in Fig. 7; asterisks denote the Fastest Growing Mode.

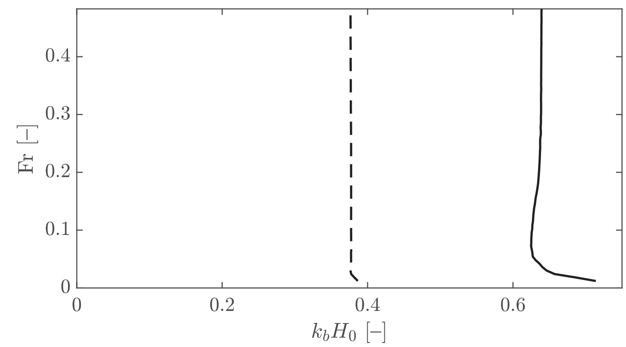

Fig. 5. Contour of zero growth rate (solid line) and the FGM (dashed line) versus the Froude number and the dimensionless wavenumber k_bH_0 (with constant relative Nikuradse roughness height $k_s^* = 1.4 \times 10^{-3}$).

for a range in Froude numbers as to compare with literature (Fig. 5). We conclude that with our nonlinear model, we can retrieve results similar as with a linear stability model: a roughly parabolic growth curve starting at the origin and reaching a maximum growth rate at the Fastest Growing Mode (FGM; e.g., Van der Sande et al., 2021). For the chosen parameters of Case I (reference case), the FGM is located at $k_b \approx 0.048\ \mathrm{m}^{-1}$ (with a corresponding wavelength of 132 m). Hence, for Case I, we expect sand dunes with wavelengths of about 132 m and migrating on the order of meters per day.

Fig. 5 shows the zero contour of the growth rate and contour of the maximum growth rate (the FGM) for a range in Froude numbers (keeping the relative Nikuradse constant at $k_s^* = 1.4 \times 10^{-3}$). Clearly, our model results barely depend on the Froude number, which is in line with the results of Richards (1980) for small Froude numbers. The contour lines are similar as those shown by Richards (1980), but are different from the results of Colombini (2004).

In sum, Figs. 4 and 5 reveal the following dependencies:

- a larger (smaller) growth rate for increased (decreased) initial flow velocity $U_{\mathrm{res},0}$, the wavelength of the FGM remains the same;
- smaller (larger) growth rate and longer (shorter) wavelength for increased (decreased) initial water depth H_0, which agrees with scaling relations from literature (Bradley and Venditti, 2017);
- larger migration rate for increasing wavenumber (decreasing wavelength), the migration rate is larger if the growth rate is larger.

The differences in growth rate motivate scaling time in displaying the morphodynamic results:

$$t^* = \frac{t}{T_m}, \qquad T_m = \frac{1}{\gamma_{r,\mathrm{FGM}}}. \tag{15}$$

Here, $\gamma_{r,\mathrm{FGM}}$ is the growth rate of the Fastest Growing Mode, indicated with an asterisk in Fig. 4. Clearly, T_m differs from run to run.

3.4. Nonlinear evolution

The morphodynamic evolution of dunes in Case I is visualized through a timestack of the bed topography using the scaled morphodynamic time as introduced in Eq. (15) (Fig. 6). Dunes grow from the initial perturbation in Eq. (7) (blue line in the upper panel of Fig. 6) to fully grown sand dunes. The dunes vary in size but are generally about one hundred meters in length, one to two meters high, and characterized by a gentle stoss slope and a steeper lee side angle. Migration rates are on the order of meters per day, which corresponds to commonly observed migration rates of river dunes (Lokin et al., 2022).

Fig. 7 shows the development of four dominant Fourier modes (the same as highlighted in Fig. 4), revealing dynamic behavior of individual modes after initial exponential growth (Fig. 7b). In the initial phase ($t^* < 2$), the dominant mode has a wavelength of 133 m (yellow line). This agrees well with the FGM as can be derived from Fig. 4. Over time,

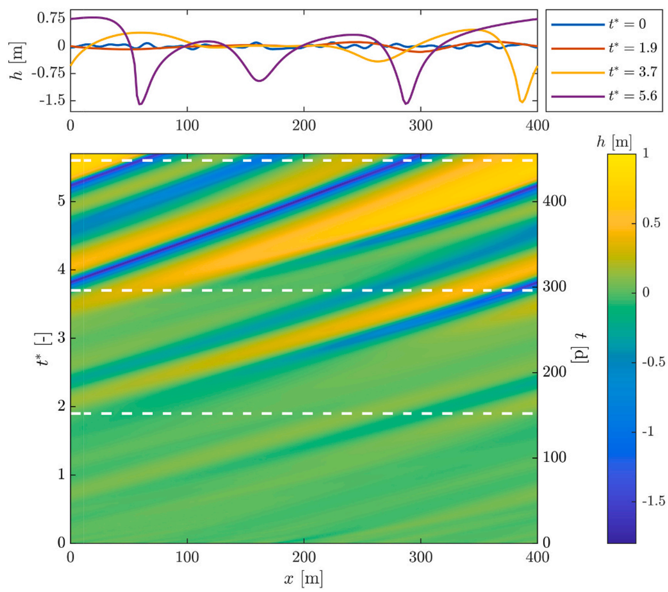

Fig. 6. Morphodynamic evolution for Case I (reference case), with the upper panel showing bed profile h at different moments in time; the lower panel shows the time stack of the topography, the white dashed lines refer to the upper panel. Time axis shows the dimensionless morphodynamic time t^* as introduced in Eq. (15) with morphodynamic timescale $T_m = 80$ d; the right vertical axis shows the corresponding time in days.

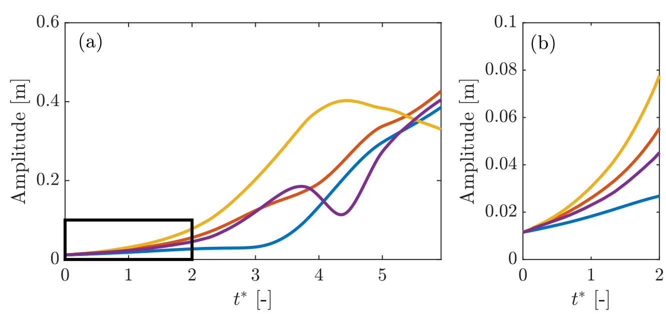

Fig. 7. (a) Amplitude development of four dominant Fourier modes $|\hat{h}_n|$ (as defined in Eq. (13), lines correspond with dots in Fig. 4) in Case I (reference case), (b) zoom of box in the lower left corner of (a) showing initially exponential or nearly exponential growth. $n \in \{1, 2, 3, 4\}$; dune wavelengths corresponding to the lines are 400 m ($n = 1$), 200 m, 133 m, 100 m ($n = 4$).

however, other modes become dominant (see also discussion, Section 4.3).

The evolution of amplitudes of topographic modes for the different parameter settings (see Table 1) is visualized in Fig. 8. Initially, for all cases the mode with the largest amplitude is around the one predicted by the FGM (Fig. 4). Over time, however, there is a tendency towards smaller wavenumbers.

Like in the linear regime, the results for different initial domain-averaged velocity $U_{\text{res},0}$ are nearly identical. This results from scaling time with the morphodynamic timescale T_m. Also in the finite amplitude regime, the flow velocity primarily changes the timescale at which the topography develops, but other than that does not significantly affect dune dynamics in the finite amplitude regime.

3.5. Modeled effective roughness

The time evolution of the spatially averaged dimensionless water depth $\frac{H}{H_0}$ (a proxy for roughness) is shown in Fig. 9 (a), revealing an increase of about 3–5 % in water depth as a result of dunes developing from a flat bed. This is further clarified in Fig. 9 (b), which shows the effective roughness height $k_{s,\text{eff}}$ as determined from the model output (Van Rijn, 1984):

$$C = \frac{U_{\text{res}}}{\sqrt{H i_b}} = 18 \log\left(\frac{12H}{k_{s,\text{eff}}}\right). \tag{16}$$

Here, U_{res} is the domain-averaged flow velocity (which varies throughout the morphodynamic evolution), C is the Chézy coefficient, and $k_{s,\text{eff}}$ denotes the effective Nikuradse roughness height. The latter is an approximation resulting from assuming a logarithmic velocity profile (following from the law of the wall) in the entire water column, and thus differs from the Nikuradse roughness height k_s in our model formulation (Table 1), which is used to apply the law of the wall only in the wall-adjacent grid cells. These results underline the significance of dune-induced form roughness on flow, with the effective roughness length increasing about 50–100 % throughout the simulation.

The increased form roughness is attributed to increased lee-side effects induced by sharp lee-side angles. The maximum angle in the domain is shown in Fig. 9 (c) and follows the trend shown in panels (a) and (b). The maximum angle grows to about 20°; we reflect on these values in Section 4.4.

Lastly, Fig. 9 (d) shows the potential energy density of sand dunes (Garnier et al., 2006):

$$E_{\text{morph}} = \frac{1}{L}\int_0^L h^2 \mathrm{d}x, \tag{17}$$

the time derivative of which is a measure of how far the system is from dynamic quasi-equilibrium. We use the term quasi-equilibrium here to refer to a sand dune field which, although not in a true mathematical equilibrium, does not change pronouncedly anymore. Clearly, the potential energy density of sand dunes develops in a similar way as the water depth and the effective roughness height. From Fig. 9 (d), it can be concluded that Case II ($H_0 = 4$ m) has reached a dynamic quasi-equilibrium at the end of the simulation, whereas this is not true for Case III ($H_0 = 10$ m).

4. Discussion

4.1. Application to the river Rhine

Here, we aim to compare our model results to an observed dune field near Dodewaard in the Waal branch of the river Rhine, The Netherlands (Lokin et al., 2023). The observations were made after a prolonged period of relatively low discharge, on August 6th 2018, with a specific discharge of $U_{\text{res}}H = 3.3\,\text{m}^2\text{s}^{-1}$ at a water depth of 4 m; the energy slope is given by $i_b = 5 \times 10^{-5}$. Here, we do not account for sediment grain size. Dunes have heights of 0.5–1.0 m, lengths of about 100–150 m, and lee side angles of maximum 5° (see solid line in upper panel of Fig. 10).

First, we choose a Nikuradse roughness height which matches the forcing $g_i \approx g i_b$ to the given specific discharge. This results in a roughness height of $k_s = 0.016$ m, which is close to the value we used before, and possibly reflects the presence of superimposed ripples at the field site.

Results – given in Fig. 10 – show that initially, relatively short dunes develop, as also predicted by the growth curve in Fig. 4 for $H = 4$ m. Over time, the patterns coarsen (i.e., dunes amalgamate) to form dunes with lengths of about 80 m, which is somewhat shorter than those observed in the field; furthermore, the modeled dunes have deeper troughs and are steeper, with lee side angles around the angle of repose. These discrepancies are further discussed in Section 4.4 in which we argue that these qualitative differences are the result of neglecting suspended sediment transport. Another assumption implicitly made here in the application to the Rhine is that we assume constant conditions and thus neglect forcing variability and hysteresis effects in the comparison.

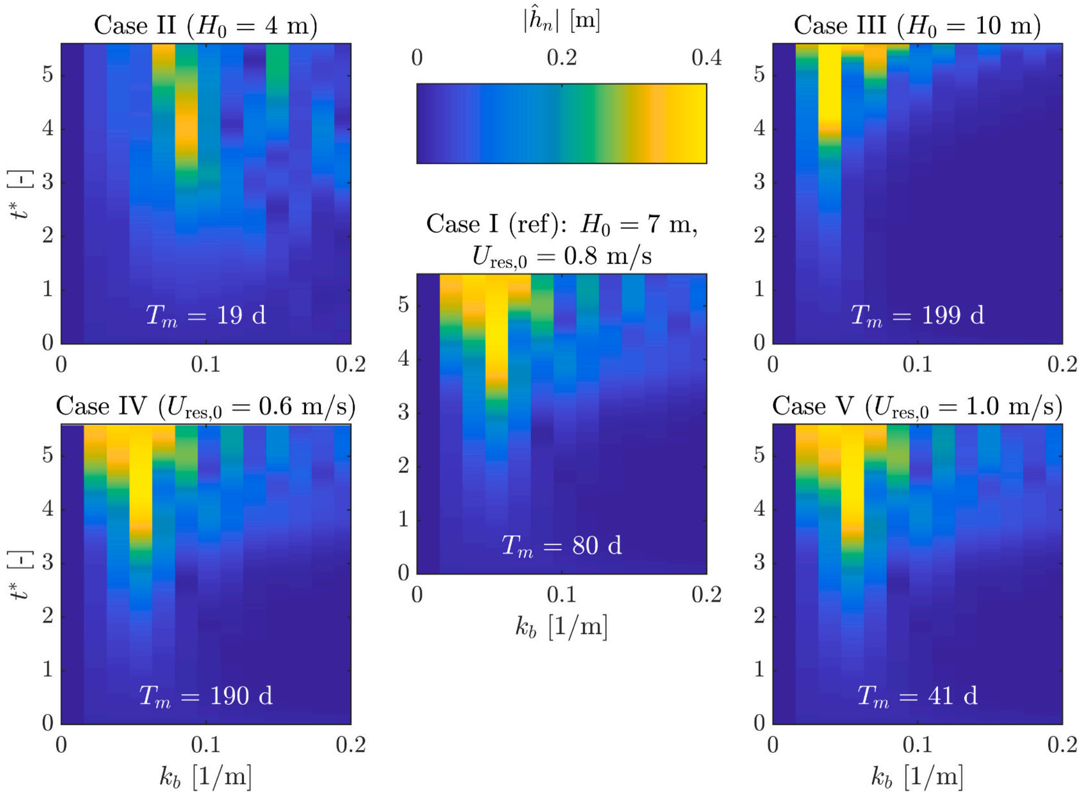

Fig. 8. Time stack of Fourier amplitudes for all cases (see Table 1 for the parameter values).

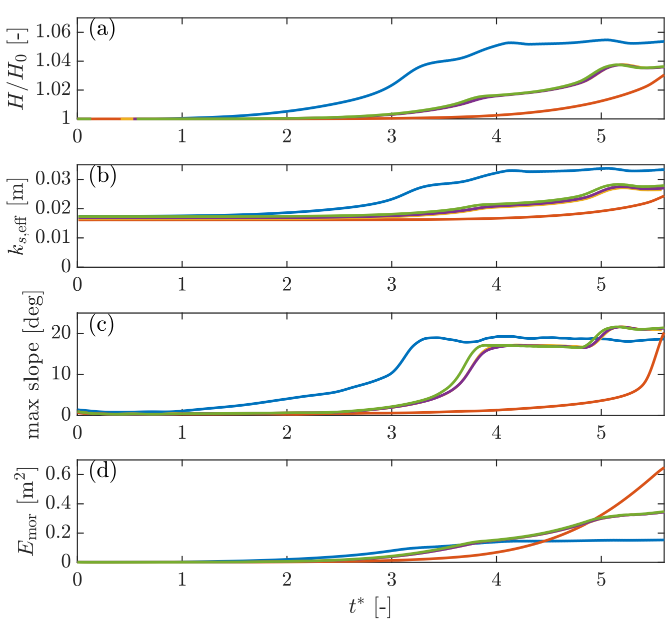

Fig. 9. Evolution of different quantities with line colors corresponding to: Case I (reference case, $H_0 = 7\,m$, $U_{\text{res},0} = 0.8\ \text{ms}^{-1}$), Case II ($H_0 = 4$ m), Case III ($H_0 = 10$ m), Case IV $\left(U_{\text{res},0} = 0.6\ \text{ms}^{-1}\right)$, Case V ($U_{\text{res},0} = 1.0\ \text{ms}^{-1}$). (a) Dimensionless water depth H/H_0; (b) modeled effective roughness length $k_{s,\text{eff}}$; (c) (smoothed) evolution of the maximum (absolute) slope in the domain; (d) E_{morph}, the potential energy density of sand dunes as defined in Eq. (17). Note that the yellow lines ($U_{\text{res},0} = 0.6\ \text{ms}^{-1}$) are not visible as they lay underneath the purple line (Case I) and green line (Case V). (For interpretation of the references to color in this figure legend, the reader is referred to the web version of this article.)

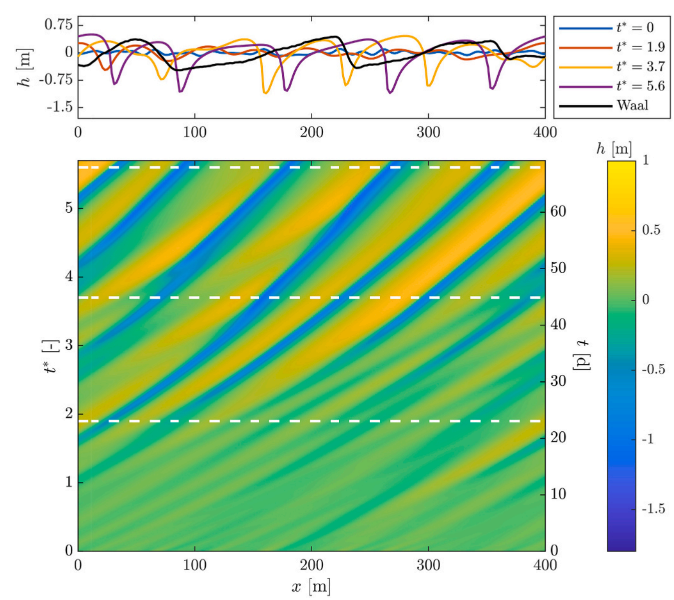

Fig. 10. Model application to the Waal branch of the river Rhine, with morphodynamic timescale $T_m = 12$ d.

These effects could be relevant, even though the observations were made after a prolonged period of relatively constant forcing. We conclude that our model is capable of producing a dune field with characteristics (length, height, shape) that roughly match those of observed sand dunes.

4.2. Formation of river dunes

The origin of river dunes has been a point of debate in the past, with one hypothesis arguing that large-scale dunes are the result of pattern coarsening of smaller-scale ripples – which in turn arise as linear instability of the flat bed (Fourrière et al., 2010; Doré et al., 2016). The other hypothesis argues that large-scale dunes originate themselves as a linear instability (Engelund, 1970; Richards, 1980; Paarlberg et al., 2009). The results in Fig. 4 show that, also with a complex nonlinear model, we can retrieve a growth curve as from linear stability models which predicts an FGM that is also dominant in the initial growth phase (Figs. 7 and 8). Hence, our results support the hypothesis that river dunes form by linear instability.

4.3. Saturated dune length

Ultra long simulations (even longer than those shown here, about 10 years) suggest that the only stable mathematical dynamic equilibrium with this setup constitutes a single dune spanning the entire domain. This is a common property of morphodynamic dune models with periodic boundary conditions, for both tidal and riverine settings (Doré et al., 2016; Campmans et al., 2018; Niemann et al., 2011). Not only is it a mere model limitation: it raises the question to what physical mechanism is responsible for setting the maximum wavelength.

The results of our model with a relatively complex flow module suggest that the adopted turbulence closure and non-hydrostaticity do not resolve the above issue of dune length. This could mean that a more detailed turbulence description such as LES is required to capture dune-dune interactions (e.g., Frias and Abad, 2013). Alternative mechanisms responsible for damping large wavelengths are suspended sediment (Bacik et al., 2020; Borsje et al., 2014), dune splitting through superimposed ripples (Warmink et al., 2014), lateral variations (i.e., three-dimensionality), or temporal variability in the forcing conditions.

4.4. Lee-angle dynamics

Dunes in our model steepen towards the angle of repose ($\Theta = 30^{\circ}$), with maximum lee side angles around 25°. Clearly, our formulation of the slope correction, given by Eq. (4), puts a limit on the steepness of dunes. Dunes in large rivers, however, typically have more gentle lee side angles (Fig. 10; Lokin et al., 2022; Cisneros et al., 2020). This discrepancy might be related to our model setup which excludes suspended sediment transport, which has been shown to lead to longer bedforms with more gentle slopes and smaller heights (Campmans et al., 2017; Van Gerwen et al., 2018; Van Duin et al., 2021).

5. Conclusion

We have presented a new morphodynamic river dune model with a hydrodynamic module that is capable of capturing lee side effects (i.e., increased turbulent kinetic energy and potentially flow separation). Indeed, as dunes develop, instances occur of flow separation and corresponding increased turbulent kinetic energy at the lee side. Furthermore, the model shows that dunes initially grow as a free instability of the flat bed, characterized by exponential growth of Fourier modes, whereas in the spatial domain growth appears to be driven by merging. In the nonlinear stage, they reach a quasi-equilibrium – with smaller topographic modes becoming more dominant over time. Hence, similar to past morphodynamic models, the presented model lacks the capacity to produce a maximum wavelength. Due to the form roughness from dunes, water depth increases about 3–5 % as dunes evolve from a flat bed; this is reflected in an increased effective roughness length.

6. Open research

The hydrodynamic module of the morphodynamic model described here is solved within OpenFOAM, v2206 (https://www.openfoam.com/news/main-news/openfoam-v2206), using the solver SimpleFOAM. The morphodynamic loop is closed with a sediment transport formula and bed evolution. The C++ code of this model is published in the following repository: https://doi.org/10.5281/zenodo.14864409.

CRediT authorship contribution statement

W.M. van der Sande Writing – review & editing, Writing – original draft, Software, Resources, Methodology, Investigation, Formal analysis, Conceptualization. **P.C. Roos:** Writing – review & editing, Supervision, Project administration, Methodology, Investigation, Funding acquisition, Formal analysis, Conceptualization. **T. Gerkema:** Writing – review & editing, Methodology, Formal analysis, Conceptualization. **S. J.M.H. Hulscher:** Writing – review & editing, Supervision, Project administration, Funding acquisition.

Declaration of competing interest

The authors declare that they have no known competing financial interests or personal relationships that could have appeared to influence the work reported in this paper.

Acknowledgements

This research is funded by the 'Simon Stevin Meester' prize (awarded by NWO to S.J.M.H. Hulscher) and the Perspectief Program SALTISolutions, which is financed by NWO Domain Applied and Engineering Sciences in collaboration with private and public partners. We thank Joost Kranenborg, Vasileios Kitsikoudis, Jord Warmink, Johan Damveld, and Geert Campmans for helpful discussions on the model setup. We thank Lieke Lokin for providing the data in Section 4.1.

Appendix A. Numerical solution procedure

First, the Exner Equation (1) is split in two terms which are treated separately:

$$(1 - p_{\mathrm{or}})\frac{\partial h}{\partial t} = \underbrace{-\alpha\frac{\partial}{\partial x}\left(|\tau_b|^{\beta-1}\tau_b\right)}_{\mathrm{I}} + \underbrace{\alpha\frac{\partial}{\partial x}\left(|\tau_b|^{\beta}\lambda\frac{\partial h}{\partial x}\right)}_{\mathrm{II}}. \tag{A.1}$$

Here, we recognize a hyperbolic term (I), and a parabolic term (II). The hyperbolic term is solved through a TVD scheme with the MinMod limiter; the parabolic slope term is discretized through a semi-implicit Crank-Nickolson scheme:

$$\frac{h_j^{n+1}-h_j^n}{\Delta t_n} = -\frac{q_{j+1/2}^n - q_{j-1/2}^n}{\Delta x} + \frac{\alpha}{\Delta x}\Bigg\{\lambda_{j+1/2}^n\left(|\tau_b|^\beta\right)_{j+1/2}^n\left[\frac{h_{j+1}^n-h_j^n}{2\Delta x}+\frac{h_{j+1}^{n+1}-h_j^{n+1}}{2\Delta x}\right] - \lambda_{j-1/2}^n\left(|\tau_b|^\beta\right)_{j-1/2}^n\left[\frac{h_j^n-h_{j-1}^n}{2\Delta x}+\frac{h_j^{n+1}-h_{j-1}^{n+1}}{2\Delta x}\right]\Bigg\}. \tag{A.2}$$

As pointed out in the main text, time is discretized with variable timestep (depending on stability criteria) as $t_n = \sum_{i=0}^{n-1}\Delta t_n$, and space as $x_j = \left(j+\frac{1}{2}\right)\Delta x$ (see Eq. (8)). Quantities at $j \pm 1/2$ are approximated as follows:

$$\left(|\tau_b|^\beta\right)_{j+1/2}^n = \frac{1}{2}\left[\left(|\tau_b|^\beta\right)_j^n + \left(|\tau_b|^\beta\right)_{j+1}^n\right], \quad \lambda_{j+1/2}^n = \lambda\left(\frac{h_{j+1}^n - h_j^n}{\Delta x}\right). \tag{A.3}$$

Lastly, the value of $q_{j+1/2}^n$ is constructed from the value at neighboring grid points j and $j+1$ with the MinMod limiter, which switches between first order upwind and central difference discretization depending on the local characteristics of the problem.

Appendix B. Numerical convergence

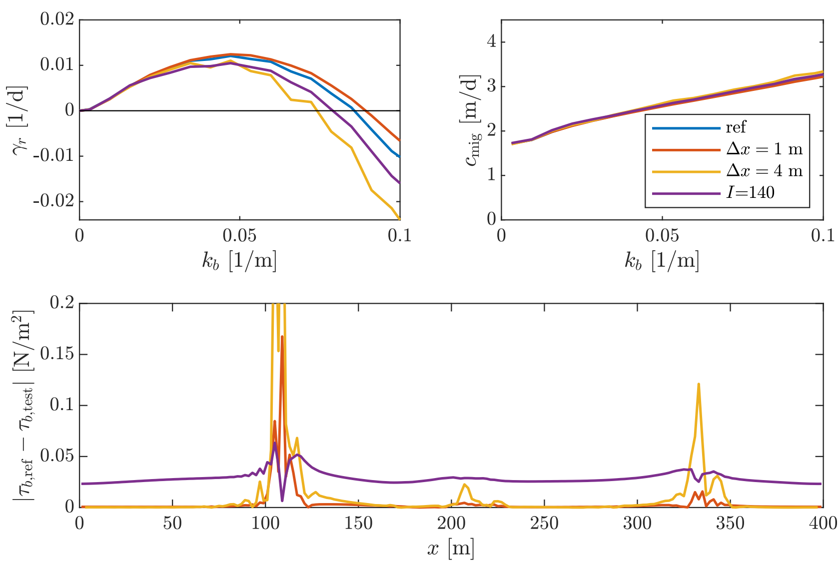

Fig. B.11. Convergence of the model results to spatial stepsize Δx and number of vertical grid cells I, shown for a growth and corresponding migration curve (upper right and upper left panel, respectively), and for bed shear stress over a developed dune field (topography at the end of the reference simulation). The values used for the reference case are $\Delta x = 2$ m and $I = 70$.

Convergence of the numerical scheme is shown through the growth and migration curves (initial dynamics) and the difference in bed shear stress over a dune field as obtained at the end of Case I (nonlinear dynamics). These are evaluated for different spatial step sizes: $\Delta x = 1$ m and $\Delta x = 4$ m (default $\Delta x = 2$ m), and for a different number of vertical grid cells: $I = 140$ (for Case I $I = 70$). Although the growth curves deviate somewhat from one another, these differences are negligible compared to changes in environmental parameters (Fig. 4), and the maxima are located approximately at the same wavenumber. The migration curves of the different runs are almost the same. Lastly, the bed shear stress over a developed topography is generally accurate, although less so over steep lee sides, over which the error is roughly 10 % (for a bed shear stress of about 1.5 Nm^{-2}).

References

Bacik, K.A., Lovett, S., Caulfield, C.C.P., Vriend, N.M., 2020. Wake induced long range repulsion of aqueous dunes. Phys. Rev. Lett. 124 (054501).
Bagnold, R.A., 1956. The flow of cohesionless grains in fluids. Philos. Trans. R. Soc. Lond. A Math. Phys. Sci. 249, 235–297.
Bardina, J.E., Huang, P.G., Coakley, T.J., 1997. Turbulence Modeling Validation, Testing, and Development. Technical Report. NASA, Mountain View.
Blondeaux, P., 1990. Sand ripples under sea waves: part 1. Ripple formation. J. Fluid Mech. 218, 1–17.
Borsje, B.W., Kranenburg, W.M., Roos, P.C., Matthieu, J., Hulscher, S.J.M.H., 2014. The role of suspended load transport in the occurrence of tidal sand waves. Case Rep. Med. 119 (4), 701–716.
Bradley, R.W., Venditti, J.G., 2017. Reevaluating dune scaling relations. Earth-Sci. Rev. 165, 356–376.
Campmans, G.H.P., Roos, P.C., de Vriend, H.J., Hulscher, S.J.M.H., 2017. Modeling the influence of storms on sand wave formation: a linear stability approach. Cont. Shelf Res. 137, 103–116.
Campmans, G.H.P., Roos, P.C., de Vriend, H.J., Hulscher, S.J.M.H., 2018. The influence of storms on sand wave evolution: a nonlinear idealized modeling approach. Case Rep. Med. 123 (9), 2070–2086.
Charru, F., Andreotti, B., Claudin, P., 2013. Sand ripples and dunes. Annu. Rev. Fluid Mech. 45, 469–493.
Cisneros, J., Best, J., van Dijk, T., de Almeida, R.P., Amsler, M., Boldt, J., Freitas, B., Galeazzi, C., Huizinga, R., Ianniruberto, M., Ma, H., Nittrouer, J.A., Oberg, K., Orfeo, O., Parsons, D., Szupiany, R., Wang, P., Zhang, Y., 2020. Dunes in the world's big rivers are characterized by low-angle lee-side slopes and a complex shape. Nat. Geosci. 13, 156–162.
Colombini, M., 2004. Revisiting the linear theory of sand dune formation. J. Fluid Mech. 502 (502), 1–16.
Colombini, M., Stocchino, A., 2008. Finite-amplitude river dunes. J. Fluid Mech. 611, 283–306.

Damen, J.M., van Dijk, T.A.G.P., Hulscher, S.J.M.H., 2018. Spatially varying environmental properties controlling observed sand wave morphology. Case Rep. Med. 123 (2), 262–280.
Damveld, J.H., Borsje, B.W., Roos, P.C., Hulscher, S.J.M.H., 2020. Horizontal and vertical sediment sorting in tidal sand waves: modeling the finite-amplitude stage. Case Rep. Med. 125 (10).
Davies, A.G., Robins, P.E., 2017. Residual flow, bedforms and sediment transport in a tidal channel modelled with variable bed roughness. Geomorphology 295, 855–872.
Dodd, N., Blondeaux, P., Calvete, D., De Swart, H.E., Falqués, A., Hulscher, S.J.M.H., Rózynski, G., Vittori, G., 2003. Understanding coastal morphodynamics using stability methods. J. Coast. Res. 19 (4), 849–865.
Doré, A., Bonneton, P., Marieu, V., Garlan, T., 2016. Numerical modeling of subaqueous sand dune morphodynamics. Case Rep. Med. 121 (3), 565–587.
Engelund, F., 1970. Instability of erodible beds. J. Fluid Mech. 42 (2), 225–244.
Fourrière, A., Claudin, P., Andreotti, B., 2010. Bedforms in a turbulent stream: formation of ripples by primary linear instability and of dunes by nonlinear pattern coarsening. J. Fluid Mech. 649, 287–328.
Frias, C.E., Abad, J.D., 2013. Mean and turbulent flow structure during the amalgamation process in fluvial bed forms. Water Resour. Res. 49, 6548–6560.
Garnier, R., Calvete, D., Falques, A., Caballeria, M., 2006. Generation and nonlinear evolution of shore-oblique-transverse sand bars. J. Fluid Mech. 567, 327–360.
Giri, S., Shimizu, Y., 2006. Numerical computation of sand dune migration with free surface flow. Water Resour. Res. 42 (10).
Giri, S., Yamaguchi, S., Nabi, M., Nelson, J., 2015. Numerical modelling of river dunes in the waal under extreme floods. In: E-proceedings 36th IAHR World Congr.
Hulscher, S.J.M.H., 1996. Tidal-induced large-scale regular bed form patterns in a three-dimensional shallow water model. J. Geophys. Res. 101 (C9), 20727–20744.
Hulscher, S.J.M.H., Dohmen-Janssen, C.M., 2005. Introduction to special section on marine sand wave and river dune dynamics. Case Rep. Med. 110 (F4).
Huthnance, J.M., 1982. On one mechanism forming linear sand banks. Estuar. Coast. Shelf Sci. 14, 79–99.
Ji, Z.G., Mendoza, C., 1997. Weakly nonlinear stability analysis for dune formation. J. Hydraul. Eng. 123 (11), 979–985.
Kostaschuk, R., 2000. A field study of turbulence and sediment dynamics over subaqueous dunes with flow separation. Sedimentology 47 (3), 519–531.
Krabbendam, J., Nnafie, A., de Swart, H., Borsje, B., Perk, L., 2021. Modelling the past and future evolution of tidal sand waves. J. Mar. Sci. Eng. 9 (10).
Kundu, P.K., Cohen, I.M., Dowling, D.R., 2016. Fluid Mechanics, 6 edition. Academic Press.
Kwoll, E., Venditti, J.G., Bradley, R.W., Winter, C., 2016. Flow structure and resistance over subaquaeous high- and low-angle dunes. Case Rep. Med. 121 (3), 545–564.
Lefebvre, A., Winter, C., 2016. Predicting bed form roughness: the influence of lee side angle. Geo-Mar. Lett. 36, 121–133.
Lefebvre, A., Paarlberg, A.J., Winter, C., 2014. Flow separation and shear stress over angle-of-repose bed forms: a numerical investigation. Water Resour. Res. 50 (2), 986–1005.
Lesser, G.R., Roelvink, J.A., van Kester, J.A.T.M., Stelling, G.S., 2004. Development and validation of a three-dimensional morphological model. Coast. Eng. 51 (8–9), 883–915.
Liu, Y., Fang, H., Huang, L., He, G., 2019. Numerical simulation of the production of three-dimensional sediment dunes. Phys. Fluids 31 (9).
Lokin, L.R., Warmink, J.J., Bomers, A., Hulscher, S.J.M.H., 2022. River dune dynamics during low flows. Geophys. Res. Lett. 49 (8).
Lokin, L.R., Warmink, J.J., Hulscher, S.J.M.H., 2023. The effect of sediment transport models on simulating river dune dynamics. Water Resour. Res. 59 (12).
Meyer-Peter, E., Müller, R., 1948. Formulas for bed-load transport. In: Rep. 2nd Meet. Int. Assoc. Hydraul. Struct. Res. IAHR, Stockholm, pp. 39–64.
Nabi, M., De Vriend, H.J., Mosselman, E., Sloff, C.J., Shimizu, Y., 2013. Detailed simulation of morphodynamics: 3. Ripples and dunes. Water Resour. Res. 49 (9), 5930–5943.
Niemann, S.L., Fredsøe, J., Jacobsen, N.G., 2011. Sand dunes in steady flow at low froude numbers: dune height evolution and flow resistance. J. Hydraul. Eng. 137 (1), 5–14.
Paarlberg, A.J., Dohmen-Janssen, C.M., Hulscher, S.J.M.H., Termes, P., 2007. A parameterization of flow separation over subaqueous dunes. Water Resour. Res. 43 (12).
Paarlberg, A.J., Dohmen-Janssen, C.M., Hulscher, S.J.M.H., Termes, P., 2009. Modeling river dune evolution using a parameterization of flow separation. Case Rep. Med. 114 (F1).
Richards, K.J., 1980. On the formation of ripples and dunes on an erodible bed. J. Fluid Mech. 99 (3), 597–618.
Sotiropoulos, F., Khosronejad, A., 2016. Sand waves in environmental flows: Insights gained by coupling large-eddy simulation with morphodynamics. Phys. Fluids 28 (2).
Trowbridge, J.H., 1995. A mechanism for the formation and maintenance of shore-oblique sand ridges on storm-dominated shelves. J. Geophys. Res. 100 (C8), 16071–16086.
Van den Berg, J., Sterlini, F., Hulscher, S.J.M.H., Van Damme, R.M.J., 2012. Non-linear process based modelling of offshore sand waves. Cont. Shelf Res. 37, 26–35.
Van der Sande, W.M., Roos, P.C., Gerkema, T., Hulscher, S.J.M.H., 2021. Gravitational circulation as driver of upstream migration of estuarine sand dunes. Geophys. Res. Lett. 48 (14).
Van der Sande, W.M., Roos, P.C., Gerkema, T., Hulscher, S.J.M.H., 2023. Shorter estuarine dunes and upstream migration due to intratidal variations in stratification. Estuar. Coast. Shelf Sci. 281.
Van Duin, O.J., Hulscher, S.J., Ribberink, J.S., 2021. Modelling regime changes of dunes to upper-stage plane bed in flumes and in rivers. Appl. Sci. 11 (23).
Van Gerwen, W., Borsje, B.W., Damveld, J.H., Hulscher, S.J.M.H., 2018. Modelling the effect of suspended load transport and tidal asymmetry on the equilibrium tidal sand wave height. Coast. Eng. 136, 56–64.
Van Rijn, L.C., 1984. Sediment transport, part III: bed forms and alluvial roughness. J. Hydraul. Eng. 110 (12), 1733–1754.
Vittori, G., Blondeaux, P., 2020. River dunes and tidal sand waves: are they generated by the same physical mechanism? Water Resour. Res. 56(5):e2019WR026800. https://doi.org/10.1029/2019WR026800 e2019WR026800.
Warmink, J.J., Dohmen-Janssen, C.M., Lansink, J., Naqshband, S., Van Duin, O.J.M., Paarlberg, A.J., Termes, P., Hulscher, S.J.M.H., 2014. Understanding river dune splitting through flume experiments and analysis of a dune evolution model. Earth Surf. Process. Landf. 39, 1208–1220.
Weller, H.G., Tabor, G., Jasak, H., Fureby, C., 1998. A tensorial approach to computational continuum mechanics using object-oriented techniques. Comput. Phys. 12 (6), 620–631.
Wilcox, D.C., 1993. Comparison of two-equation turbulence models for boundary layers with pressure gradient. AIAA J. 31 (8), 1414–1421.
Xie, Z., Lin, B., Falconer, R.A., Maddux, T.B., 2013. Large-eddy simulation of turbulent open-channel flow over three-dimensional dunes. J. Hydraul. Res. 51 (5), 494–505.